Patient-Specific In-vivo Dynamic Motion of Ascending Thoracic Aortic Aneurysms from Cine CTA

Rodrigo Valente, André Mourato, Alda Carvalho, José Xavier, Moisés Brito, Stéphane Avril, António Tomás, José Fragata

***Abstract*— Ascending Thoracic Aortic Aneurysm (ATAA) is a potentially fatal cardiovascular condition that may result in dissection or rupture. As a general rule, current guidelines recommend surgical intervention when the aneurysm diameter exceeds a critical threshold, typically around 55 mm in average-risk patients. However, acute complications have been reported in patients with smaller aneurysms, underscoring the need for more accurate and individualised risk stratification criteria. In this work, we propose a novel method to extract the motion of the ATAA from Cine Computed Tomography Angiography (cCTA) data, enabling the derivation of multiple motion-related variables and the assessment of their clinical significance. This method involves a multi-view 2D U-Net segmentation, followed by an algorithm to calculate nodal deformation between independent segmentations at each time-step of the cardiac cycle. The motion is described generally across the ATAA and then specifically focused on the Aortic Root (AR). The analysis was performed on 82 patients and, afterwards, a Principal Component Analysis (PCA) was performed on 28 metrics to understand which have a relevant impact on inter-patient variability. This showed that mean pressure, weight and centreline length are the most relevant variables to understand patient's variability considering PCA loadings. These results can offer new insights into ATAA biomechanics, supporting the development of future risk stratification models and clinical decision-making.**

***Index Terms*— Ascending Thoracic Aortic Aneurysm (ATAA); Cine Computed Tomography Angiography (cCTA); Aortic Root Motion; Deformation Registration.**

Paper submited in XXXXXX. This research was funded by the Portuguese Foundation for Science and Technology (FCT,IP) under the projects: "Fluid-structure interaction for functional assessment of ascending aortic aneurysms: a biomechanical-based approach toward clinical practice", DOI: 10.54499/PTDC/EMD-EMD/1230/2021; UID/00667: Unidade de Investigação e Desenvolvimento em Engenharia Mecânica e Industrial (UNIDEMI); A.C. supported by UID/06522/2025: CEMAPRE/ISEG Research; PhD grants awarded to R.V. (2022.12223.BD) and A.M. (UI/BD/151212/2021).

R.V., A.M., J.X., M.B are with Research Unit of the Department of Mechanical and Industrial Engineering of the Faculdade de Ciências e Tecnologia da Universidade NOVA de Lisboa, Caparica, Portugal (e-mail: rb.valente@campus.fct.unl.pt; jmc.xavier@fct.unl.pt).

A.C is with DCeT, Universidade Aberta, Lisbon, Portugal and CEMAPRE/ISEG Research, Universidade de Lisboa, Lisbon, Portugal.

J.X., M.B are with Laboratório Associado de Sistemas Inteligentes - LASI, Guimarães, Portugal

S.A. is with Mines Saint-Etienne, University of Lyon, Inserm, Sainbiose U1059, Saint-Etienne, F-42023, France

A.T., J.F. are with Department of Cardiothoracic Surgery, Santa Marta Hospital, Rua de Santa Marta, Santo António, Lisboa, Portugal

J.F. is with Department of Surgery and Human Morphology, NOVA Medical School, Campo Mártires da Pátria, 1169-056 Lisboa, Portugal

I. Introduction

The Ascending Thoracic Aortic Aneurysm (ATAA) is an abnormal dilation of the initial segment of the largest artery in the human body, affecting approximately 1 individual per $10,000$ people annually [1, 2]. Such pathological deformations are suspected to arise as a consequence of ageing, environmental factors, lifestyle or medical conditions that compromise the arterial wall microstructure [3, 4]. Over time, these factors may lead to structural alterations in the vessel wall, including reduced elasticity, which in turn can promote localised enlargement. Guidelines suggest that an enlargement of the ascending aorta diameter by at least 50% relative to its normal healthy dimensions is classified as ATAA [5–7]. In the absence of other risk factors, surgical intervention is recommended when the aneurysm diameter exceeds 55 mm in men and 50 mm in women, [5]. While this simple geometric criterion provided a practical threshold, it has long been recognized as insufficient. More recently, updated international guidelines have begun to incorporate relevant patient information and additional metrics, categorizing them by "classes of recommendation" for clinical intervention (such as valve morphology, age, and patient size) [8, 9]. Nevertheless, these recommendations remain largely geometry-based since maximum diameter continues to be a main decisive recommendation factor.

Dynamic behaviour of the ATAA has gained attention as a meaningful indicator of biomechanical vulnerability. In vivo deformation metrics capture functional properties that static diameter measurements cannot. Multiphase Cine Computed Tomography Angiography (cCTA) and related imaging approaches have shown that regional stiffness and deformation patterns distinguish dilated from non-dilated aortas and relate to biomechanical stability [10, 11]. Furthermore, metrics such as the distensibility coefficient have been identified as superior predictors of failure risk compared to geometry alone [12]. Building on this perspective, several methodological advances have been proposed to better characterise ATAA mechanics. These include three-dimensional evaluations of stiffness and longitudinal growth [13], and cCTA analyses of axial length, effective diameter, and centreline curvature across the cardiac cycle [14]. Collectively, these studies underscore a shift from

purely geometry-based descriptions toward dynamic, patient-specific assessment of ATAA biomechanics, supporting the view that deformation metrics are essential for improving risk stratification. Nonetheless, most existing works either consider a limited set of motion descriptors, only have access to two timesteps (systole and diastole normally), or focus on relatively small, non-stratified cohorts, leaving open the question of how detailed ATAA and Aortic Root (AR) deformation patterns relate to clinical and geometric characteristics across different patient subgroups.

This work aims to characterise patient-specific ATAA dynamics from cCTA and to relate these motions to geometric and clinical descriptors across a clinical cohort. We build on a deep-learning and registration-based framework to obtain detailed ATAA and AR deformation over the cardiac cycle in 82 patients, and we define a set of dynamic and morphological metrics that capture both global ATAA motion and local root behaviour. To identify which metrics best explain inter-patient variability, we applied Principal Component Analysis (PCA) as an unsupervised exploratory tool to determine the combinations of dynamic, geometric, and clinical variables that most strongly characterise differences between patients. Together, this provides a comprehensive, motion-informed description of ATAA biomechanics that complements existing diameter-based criteria and may guide the development of more refined risk stratification strategies.

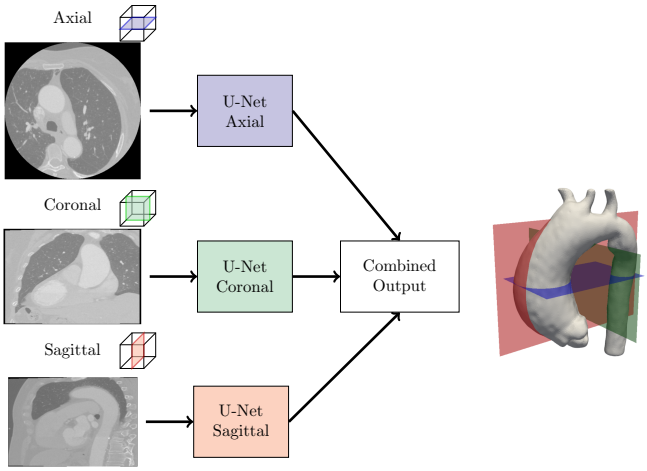

Fig. 1: Multi-view 2D U-Net pipeline. Axial, coronal, Sagittal cCTA slices independently analysed though a U-Net for a combined output.

II. Methods

A. Materials: Patients Imaging

Data for this study were collected from 82 patients diagnosed with ATAA at Hospital de Santa Marta, Lisbon, Portugal. The patients were selected based on the presence of ATAA and underwent a comprehensive clinical assessment. Metrics obtained by the physicians included weight, height, age, sex, Body Mass Index (BMI), Body Surface Area (BSA), systolic and diastolic blood pressure, heart rate, and aortic valve morphology and function, along with other relevant clinical variables. Furthermore, each patient underwent ECG gated cCTA and clinical consultations to evaluate the condition of the ATAA. The anonymised imaging datasets, obtained through ethically approved protocols under the AneurysmTool project (DOI:10.54499/PTDC/EMD-EMD/1230/2021) and approved by the board of the Unidade Local de Saúde de São José, were used to extract anatomical and dynamical features of the aorta. All participants provided written informed consent. cCTA is an imaging technique that captures cardiovascular motion across multiple cardiac cycles using ECG-gating. It reconstructs images at specific time steps (every 5% of the cardiac cycle) by combining data from several heartbeats. This allows for the assessment of ATAA deformation and displacement, providing insights into aneurysm progression.

The quality of the images obtained by the cCTA was crucial for accurate segmentation and analysis. All scans were performed on an Aquilion ONE scanner (Toshiba Medical Systems, Tochigi, Japan), which provides high-resolution imaging with thin-slice acquisition and a spatial resolution of $0.49\ \mathrm{mm} \times 0.49\ \mathrm{mm} \times 0.625\ \mathrm{mm}$. The acquisition was carried out using a low-dose radiation protocol ($100\ \mathrm{kV}$, $200\ \mathrm{mA\,s}$) and a rotation time of $0.35\ \mathrm{s}$. The process was synchronised with the electrocardiogram and performed during contrast injection (Iomeron 400, Bracco Imaging, Milan, Italy) at an injection rate of $5\ \mathrm{mL\,s^{-1}}$. The acquisition covered a field of view of $320\ \mathrm{mm}$ and used a 512×512 pixel matrix.

B. Segmentation process

Accurately capturing aortic deformation is essential for improving risk assessment and understanding the biomechanics of ATAA. While traditional methods rely on human assumptions or interaction, deep learning methods offer a data-driven alternative [15, 16]. U-Net's encoder-decoder architecture is an excellent starting point for medical image segmentation [17]. A full 3D U-Net is a gold standard of arterial segmentation but, due to high memory demands, it becomes impractical for routine use [17–19], while 2D and 2.5D approaches may fail to fully capture geometric features like curvature and the aortic valve [18, 20]. To mitigate the memory limitations without compromising 3D information, we adopted a 2D multi-view U-Net (Fig. 1). Three networks with identical architecture were independently trained for the axial, coronal, and sagittal planes to balance segmentation accuracy and computational efficiency [21]A consensus-based voting system, in which a voxel is classified as vessel if at least two views label it as foreground, then integrates the segmentations from each view, enhancing robustness and reducing errors compared to single-plane methods.

The U-Net architecture implemented on each plane is a symmetric encoder-decoder network, as illustrated in Fig. 2. The encoder consists of four downsampling blocks, each incorporating two 3×3 convolutional layers with L2 regularization ($\lambda = 0.001$), batch normalization, and ReLU activation. Each block is followed by max-pooling and progressively increasing

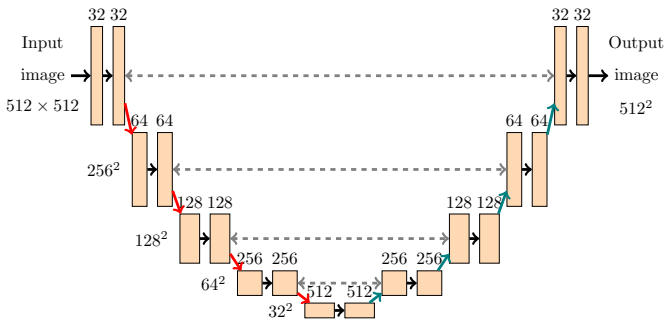

Fig. 2: Architecture of the 2D U-Net used for each view, illustrated here for the axial branch.

dropout rates (0.1-0.4) to mitigate overfitting, resulting in a network with $7,771,297$ parameters, of which $7,765,409$ are trainable.

The loss function (L) was defined as an a combination of the Binary Cross-Entropy (BCE) loss and the Dice loss, given respectively by the following expressions:

$$\text{BCE}(y_{\text{true}}, y) = -\left[y_{\text{true}} \log(y) + (1 - y_{\text{true}}) \log(1 - y)\right] \quad (1)$$

$$\text{Dice Loss}(y_{\text{true}}, y) = 1 - \frac{2 \sum (y_{\text{true}} \cdot y) + \mathit{smooth}}{\sum y_{\text{true}} + \sum y + \mathit{smooth}} \quad (2)$$

where *smooth* was set to 1. The total loss used for training each network was defined as $L = 0.5\,\text{BCE} + 0.5\,\text{Dice Loss}$, computed over each mini-batch. Upon completion of the segmentation, a Taubin smoothing algorithm was applied to the resulting surface mesh, yielding a refined and realistic appearance.

2) Semi-automatic threshold segmentation: The training procedure was developed using patient-specific segmentations obtained with a semi-automatic threshold-based segmentation algorithm [11]. This method was implemented using the scikit-image [22] and PyVista libraries [23]. The segmentation process begins with the selection of an intensity threshold and two reference points (ascending and descending aorta). Afterwards, a combination of advanced image processing techniques is applied, including watershed, binary erosion and dilation operations, as well as the morphological Chan-Vese method, to accurately define the Region of interest (ROI) in each slice. The mask in each slice is then used to initialise segmentation in the adjacent slices to improve accuracy and consistency. To finalise the segmentation, the same Taubin smoothing algorithm is applied to the mesh. This comprehensive semi-automatic approach balances the precision of manual segmentation with the efficiency of automated methods.

To analyse the quality of the segmentations, 6 patients with 2 time steps each (12 segmentations in total) were selected without criteria for comparison with hand-made segmentations. These segmentations were performed by cardiologists and the research team and they were based on threshold selection in the slicer 3D software. The Dice coefficient and Hausdorff distance were used to compare the segmentations. The Dice coefficient is a metric used to compare two volumes to evaluate the overlap between them. It is calculated using the formula presented:

$$\text{Dice coefficient} = \frac{2|A \cap B|}{|A| + |B|} \quad (3)$$

where A and B are the volumes being compared. The Dice coefficient ranges from 0 to 1, where 0 indicates no overlap and 1 indicates complete overlap.

The Hausdorff distance is another metric used to evaluate the similarity between two volumes by measuring the greatest distance between corresponding points in the two sets. A lower Hausdorff distance indicates a better match between the segmentations. The Hausdorff distance is calculated as:

$$\text{Hausdorff} = \max\left(\sup_{a \in A} \inf_{b \in B} d(a,b), \sup_{b \in B} \inf_{a \in A} d(a,b)\right) \quad (4)$$

where $d(a,b)$ is the Euclidean distance between points $a \in A$ and $b \in B$.

To analyse the quality of the semi-automatic segmentations, two arbitrary time steps for six patients (12 segmentations in total) were selected and compared with hand-made segmentations. These reference segmentations were performed by cardiologists and the research team using threshold selection in the 3D Slicer software. Our semi-automatic threshold segmentation process yielded a Dice coefficient of 0.977 $(\text{SD} = 0.004)$ and a Hausdorff distance of 0.389 mm $(\text{SD} = 0.073$ mm).

3) Training procedure: The multi-view 2D U-Net was trained on 40 segmentations (all from distinct patients to maximise anatomical variability) with 3D volume shapes of $(512, 512, 352)$, resulting in 14,080 images in the axial direction and 20,480 in coronal and sagittal. A patient-wise data split was used, with 20% of the patients reserved for validation. All images underwent preprocessing consisting of intensity normalisation and axis standardisation (consistent image size and orientation). The training was conducted with a batch size of 8, using the Adam optimiser with an exponential learning rate ranging from 1×10^{-4} to 1×10^{-8}. The networks were trained from scratch for a maximum of 600 epochs, or until early stopping was triggered if no improvements in the loss function were observed for 25 consecutive epochs. Training was performed on an NVIDIA RTX 3060 GPU with 12 GB of VRAM. The validation loss reached 0.0330 in the axial direction, 0.0303 in the coronal direction, and 0.0292 in the sagittal direction, with early stopping occurring after approximately 500 epochs.

To validate the multi-view 2D U-Net model, the same metrics as in the semi-automatic method validation process were used. The same 12 segmentations, which did not belong to the training data, served as the test set. The final multi-view 2D U-Net model presented a Dice coefficient of 0.959 $(\text{SD} = 0.005)$ and a Hausdorff distance of 0.656 mm $(\text{SD} = 0.085$ mm) when compared to the hand-made segmentations. When compared to the semi-automatic results, the U-Net achieved a Dice coefficient of 0.979 $(\text{SD} = 0.002)$ and a Hausdorff distance of 0.353 mm $(\text{SD} = 0.036$ mm).

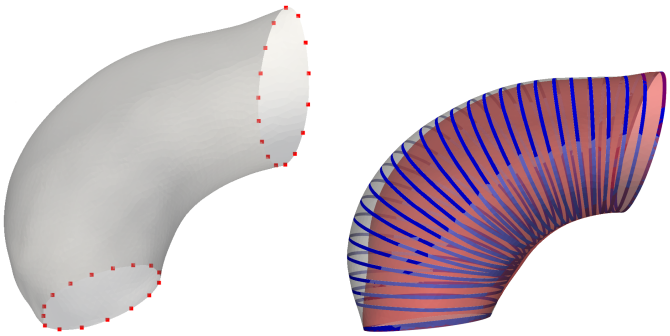

(a) Points used for the non-rigid motion calculation.

(b) Points selected for radial expansion-contraction.

Fig. 3: Points used in the ATAA to calculate the RBF non-linear deformation.

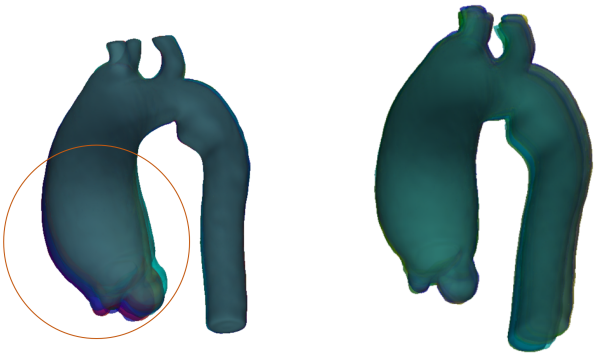

(a) 21 volumes of a single patient superimposed before RANSAC registration using the valve region as reference.

(b) 21 volumes of a single patient superimposed after ICP transformation.

Fig. 4: RANSAC point-to-plane registration process. The complete thoracic aorta is shown to visualise the deformation caused by rigid body motion.

C. Deformation calculation

The nodal deformation represents the displacement vector of each mesh node between consecutive segmentations, quantifying the local motion of the vessel wall over time. It is computed by mapping each node from the reference segmentation to its corresponding position in the target segmentation using the tracking algorithm, capturing both magnitude and direction of deformation for subsequent biomechanical analysis.

The motion of the aorta across the cardiac cycle is significant and complex. To measure the ATAA motion, it is convenient to separate it into two main deformation components. The first one corresponds to a large non-rigid body motion caused by heart contraction, which is used to align the centrelines in all volumes. The second one is represented by a predominantly radial motion in all sections caused by arterial pressure. The segmentation corresponding to the beginning of systole (0% of the cardiac cycle) was used as the reference to calculate the nodal deformation across the 21 different time volumes.

Both processes take advantage of the centreline construction using VMTK [24]. The sinotubular plane (plane that separates the aortic valve from the ATAA) and the ascending-arch junction were manually defined.

1) First step: Large non-rigid motion calculation: The large non-rigid motion refers to the motion of the sinotubular plane across space. A Radial Basis Function (RBF)-based displacement field was used to represent this deformation, defined from two sets of control points: the first in the ascending-arch junction and the second in the sinotubular plane (Fig. 3a).

Due to the ATAA behaviour, two sets of points were selected. The first group is defined by 16 points equally spaced in the plane that separates the ATAA from the aortic arch. This plane is considered fixed in space [25], thus the points are only subjected to a radial deformation defined as follows:

$$\mathbf{u}(x_j) = \big[(\mathbf{y} - \mathbf{x}_j) \cdot \hat{\mathbf{r}}(x_j)\big]\hat{\mathbf{r}}(x_j) \tag{5}$$

where $\hat{\mathbf{r}}(x_j)$ is the radial unit vector from the centreline that passes through the point $\mathbf{x}_j$, and $\mathbf{y}$ is the closest point on the target surface.

For the second set of 16 points in the sinotubular plane, the aortic valve is used as a reference to align the sinotubular plane across time.For this purpose, an Iterative Closest Point (ICP) registration method with a Random Sample Consensus model (RANSAC)-based point-to-plane metric was applied. Fig. 4 shows the ATAA of a single patient at multiple time points before and after the RANSAC registration process. After the alignment, the sinotubular plane was defined manually in the transformed configuration.

In the transformed position, a similar radial deformation is applied. Therefore, the total deformation of the current set of points is defined by:

$$\mathbf{u}'(x_k) = \big[(\mathbf{y} - \mathbf{x'}_k) \cdot \hat{\mathbf{r}}(x'_k)\big]\hat{\mathbf{r}}(x'_k) + (\mathbf{x'}_k - \mathbf{x}_k) \tag{6}$$

where the points $\mathbf{x'}_k$ are defined by $T\mathbf{x}_k$, with T being the ICP transformation matrix.

The complete large non-rigid deformation is then transferred to the rest of the mesh through an RBF interpolation, yielding a partially deformed ATAA in which the 20 centrelines present little to no residual motion across time.

2) Second step: Radial expansion-contraction: The second step in calculating the nodal deformation is to estimate the ATAA radial deformation. For that purpose, an RBF interpolation method was again used.

This step relies on multiple points inserted in rings equally spaced along the ATAA and perpendicular to the centreline. In Fig. 3b, the rings and associated points are presented. The deformation at those points is measured through Equation 5. Afterwards, a complete RBF interpolation is applied to obtain a smooth radial displacement field over the entire ATAA.

Finally, the displacements from the first and second steps are added to obtain the final deformation in all nodal points. This process was repeated for all patients, resulting in a dataset containing the nodal deformation of the ATAA for each patient.

The accuracy of the tracking algorithm was evaluated through synthetic validation. Three significant deformations

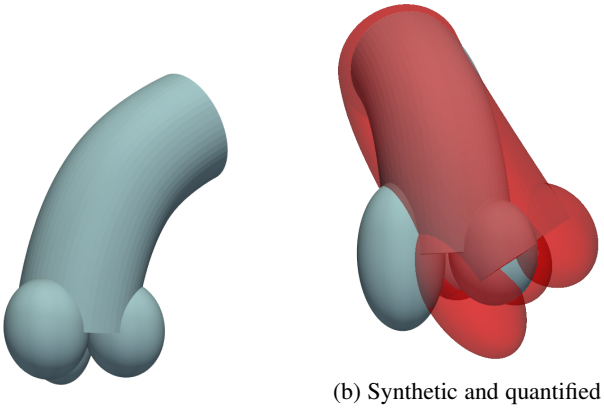

(a) Theoretical ATA created to be used as a reference.

(b) Synthetic and quantified deformation applied to theoretical ATA.

Fig. 5: Synthetic ATA created to validate the deformation method presented.

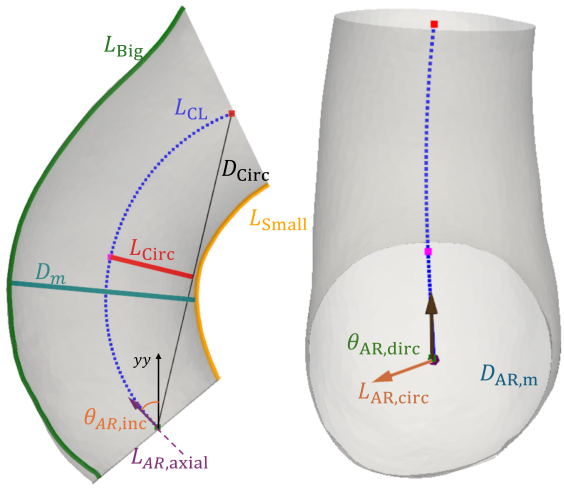

Fig. 6: Metrics defined to study ATAA dynamics. In the image: Big arc length (L_{Big}), Length of the centreline (L_{CL}), Direct length of the centreline (D_{Circ}), Small arc length (L_{Small}), Centreline arc Furthest distance (L_{Circ}), Maximum Diameter (D_{m}), AR inclination angle ($\theta_{\mathrm{AR,incr}}$), AR Axial motion ($L_{\mathrm{AR,axial}}$), AR circular motion ($L_{\mathrm{AR,circ}}$), AR motion angle ($\theta_{\mathrm{AR,direc}}$), AR maximum diameter ($D_{\mathrm{AR,m}}$).

were applied to theoretical Ascending Thoracic Aorta (ATA) geometries designed to be similar to a normal aorta (Fig. 5a), with constant radii of 16, 17, and 18 mm as presented in Figure 5b. The deformation was introduced along the centreline, with the starting point fixed at the aortic arch, while the sinotubular junction was displaced by approximately 15 mm in all in-plane directions. Subsequently, the deformation method was applied to compare the original synthetic models with their deformed targets. The Dice coefficient between the deformations and the targets was 0.996 ± 0.0006, indicating excellent overlap. The average radius difference throughout the ATA was 0.030 ± 0.0151 mm.

D. Deformation metrics

To systematically assess patient-specific characteristics, we defined a set of biomechanical metrics, together with the previously described demographic variables, to relate ATAA biomechanics to clinical status. In this study, the majority of the metrics were evaluated only at systole (35% of the cycle) and diastole (75% of the cycle), and their phase-to-phase variation was summarized as ΔX.

To compare to the benchmark of ATAA, the maximum diameter (D_{m}) and the volume (V) were measured. Furthermore, to relate the deformation with the pressure, the area distensibility ($\mathrm{Dist}_{\mathrm{Area}}$) and volume distensibility ($\mathrm{Dist}_{\mathrm{Vol}}$) were computed as follows [12]:

$$\text{Distensibility } (\mathrm{Dist}_X) = \frac{X_{\mathrm{syst}} - X_{\mathrm{dias}}}{X_{\mathrm{dias}} \cdot (P_{\mathrm{Syst}} - P_{\mathrm{Dist}})} \tag{7}$$

where X stands for the area or volume and P defines the arterial pressure in systole and diastole.

Aorta Size Index (ASI) is a relevant metric used to compare the aorta size with the body size. The ASI is calculated as follows:

$$ASI = \frac{D_{\mathrm{m}}}{BSA} \tag{8}$$

To evaluate the longitudinal behaviour of the aorta, the relative centreline length (L_{CL}) was analysed, reflecting the relative extension occurring during the cardiac cycle. Additionally, arc-length-based metrics were employed to quantify localised geometric changes, namely the small and big arc lengths (L_{Small}, L_{Big}), measured in the plane defined by the centreline centre, end, and middle points. These arc lengths serve as indirect indicators of centreline curvature.

For the analysis, the direct length of the centreline (D_{Circ}) and the distance to the furthest point between $D_{\mathrm{Circ}}$and the centreline arc (L_{Circ}) were measured. Fig. 6 provides visual support for the defined metrics. Centreline rotation, representing the torsional deformation component around the centreline axis, was also examined ($\theta_{\mathrm{CL,rot}}$).

The AR inclination angle ($\theta_{\mathrm{AR,incr}}$) was assessed, representing the tilt of the AR with respect to a reference anatomical plane (yy). This angle may play a crucial role in understanding geometric predisposition and stress. The AR centre of mass motion between systole and diastole was also analysed in the axial direction ($L_{\mathrm{AR,axial}}$), and in the circumferential plane in magnitude ($L_{\mathrm{AR,circ}}$) and direction ($\theta_{\mathrm{AR,direc}}$). The circumferential direction is measured between the AR motion vector and the projection of the centreline, as presented in Fig. 6.

The dataset contained 37 metrics. Because the majority were measured in systolic, diastolic, and peak-to-peak variation forms, strong correlations were expected. Given the nature of the variables, Pearson's linear correlation was used to identify redundant variables. For any pair with $|r| > 0.9$, the systolic metric was retained, since it normally presents the more relevant absolute values. This reduced the set to 28 metrics.

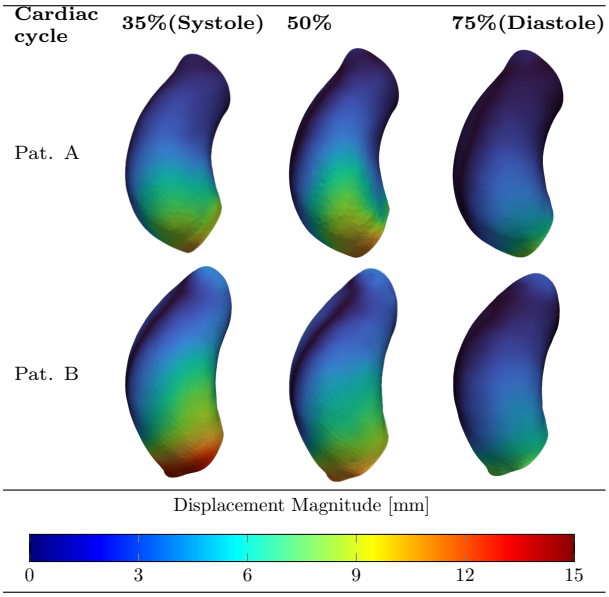

Fig. 7: Two patients as examples for the typical patient-specific deformation magnitude obtained by the deformation tracking algorithm.

E. Principal Component Analysis

PCA is a statistical technique for reducing dimensionality while retaining as much variability as possible [26]. Here, PCA was used solely as an unsupervised exploratory method to decompose the variance of 28 preselected biomechanical and clinical metrics across 82 patients, identifying which combinations of metrics (principal components) most strongly explain inter-patient variability. The analysis did not involve developing or validating any predictive classification, assigning risk categories, or correlating components with rupture or outcome events. This method was implemented using the R programming language to investigate the relationships between various patient characteristics and biomechanical metrics.

III. Results

A. Deformation measured

Fig. 7 illustrates the deformation measured in two patients at three representative time points across the cardiac cycle: systole, end of systole, and diastole. To interpret the ATAA motion, it was decomposed into two components: a radial deformation caused by pressure variation and a non-rigid body motion driven by the heart. The radial motion is present along the entire aorta but, in the ascending segment, its impact is smaller when compared with the global body motion, which is particularly evident in systole.

The AR exhibits a complex motion due to its connection with the heart. This region plays an important role in numerical models. We decomposed the AR centre of mass motion into an axial component and a radial component (taking the centreline as reference). As shown in Fig. 8, the AR centre of mass follows an elliptical trajectory in the clockwise direction, from

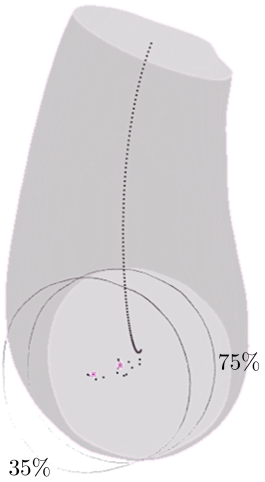

Fig. 8: AR centre of mass position over time and shape on the 35% and 75% of the cardiac cycle obtained from patient-specific data.

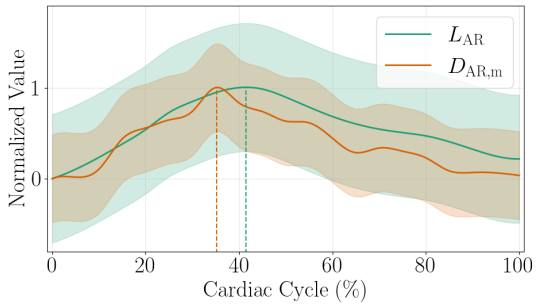

Fig. 9: Magnitude of the AR centre of mass motion and AR maximum diameter over time.

which the direction and magnitude ($L_{\mathrm{AR,circ}}$, $\theta_{\mathrm{AR,direc}}$) were calculated. The axial motion, $L_{\mathrm{AR,axial}}$, is directed towards the heart as a consequence of cardiac contraction.

Fig. 9 shows the normalised mean and Standard Deviation (SD) of the AR centre of mass displacement magnitude (combination of $L_{\mathrm{AR,circ}}$and $L_{\mathrm{AR,axial}}$) and of the AR maximum diameter ($\delta D_{\mathrm{AR,m}}$) across time. The $\delta D_{\mathrm{AR,m}}$curve reaches its maximum earlier in the cardiac cycle, whereas the centre of mass motion is more temporally distributed.

B. Biomarkers analysis

In Fig. 10, the distribution of sex and age among the patients included in this study is presented. The data reveal an uneven patient distribution, more prevalent in older age groups. Male patients are predominant, except in the 40-50 age group. Regarding aortic valve pathology, we observe that Bicuspid Aortic Valve (BAV) are predominant in younger patients suggesting that ATAA tends to develop earlier in individuals with a BAV.

Table I summarises the characteristics mentioned previously of the study population separated in different age groups. In this table the main analysed metrics are presented.

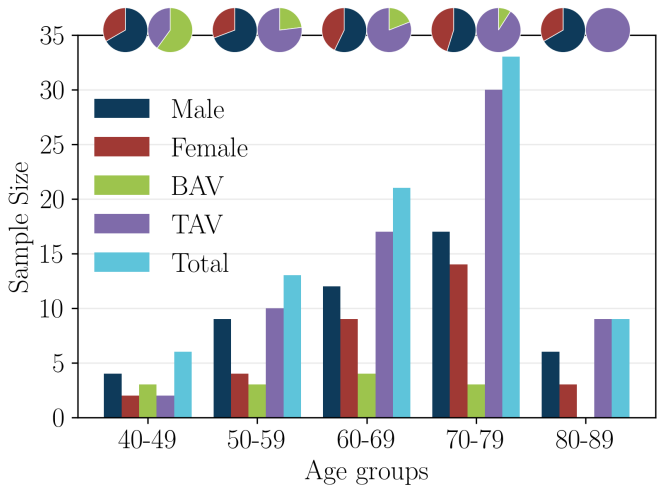

Fig. 10: Patient's sex, age and aortic valve morphology distribution.

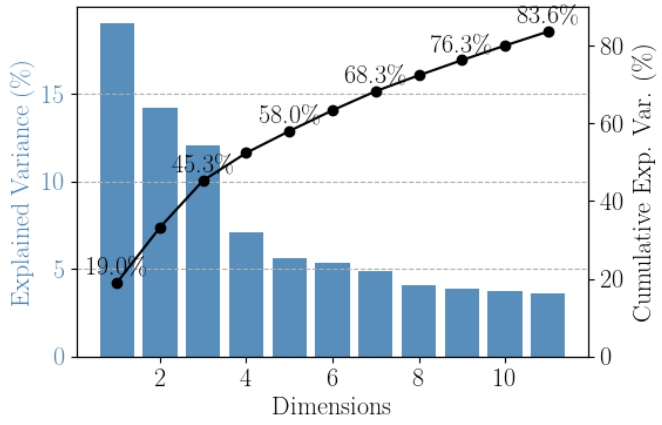

Fig. 11: Explained Variance and Cumulative Explained Variance for each of the Principal Components that respect the Kaiser criterion.

Aortic dimensions, including D_{m} and ASI, remain relatively consistent across age groups, while dynamic parameters such as $\Delta D_{\mathrm{m}}$and ΔVtend to decrease with age. Nonetheless, the small sample size in the younger age groups limits the statistical power to confirm this trend. Additionally, differences in arc-length metrics and AR motion indicate subtle variations in aortic geometry and movement patterns across age groups. Furthermore, the SD values show substantial variability within each age group for several metrics, suggesting that age alone is not sufficient to explain the observed differences.

A common rule is the Kaiser criterion, which suggests keeping only components with eigenvalues larger than one ($\lambda_k > 1$), as they explain more variance than an individual standardised variable. With these 11 dimensions, approximately 83.6% of the variance is explained. Fig. 11 shows the contribution of each selected dimension to the total explained variance.

The impact of each metric on each dimension is shown in Fig. 12. The first dimension is mainly driven by metrics that evaluate the dynamic behaviour of the ATAA and its volume, the second dimension is affected by some metrics related to the ATAA geometry (arc lengths L_{Small}, L_{Big}), the third and fourth components are more related to the size of the patient and blood pressure, respectively.

Fig. 13 shows the global impact for each dimension. Higher w_j values indicate that a variable is better represented in the reduced PCA space, meaning its variability is well captured by the principal components. The top five metrics according to this criterion are P_{Mean}, weight, L_{CL}, ASI, and L_{Circ}.

TABLE I: Patient-specific characteristics organized in aged groups with Mean and Standard deviation ($\pm$ SD).

Data	**40-49**	**50-59**	**60-69**	**70-79**	**80-89**	**All**
Sample Size	6	13	21	33	9	82
Sex (M) [%]	66.67	69.23	57.14	57.58	66.67	60.98
Fam. Hist. [%]	33.33	0.00	4.76	6.06	11.11	7.32
BAV [%]	66.67	23.08	19.05	9.09	0.00	17.07
BMI [$\mathrm{kg\,m^{-2}}$]	27.21 $\pm$4.92	28.73 $\pm$3.65	28.79 $\pm$5.11	26.91 $\pm$4.52	25.93 $\pm$5.96	27.59 $\pm$4.75
BSA [$\mathrm{m^2}$]	1.88 $\pm$0.27	1.84 $\pm$0.12	1.93 $\pm$0.18	1.82 $\pm$0.23	1.81 $\pm$0.20	1.86 $\pm$0.20
ASI [$\mathrm{cm\,m^{-2}}$]	2.68 $\pm$0.51	2.74 $\pm$0.23	2.67 $\pm$0.36	2.76 $\pm$0.41	2.99 $\pm$0.46	2.75 $\pm$0.39
HR [BPM]	64.67 $\pm$6.95	65.08 $\pm$9.80	65.86 $\pm$7.04	64.61 $\pm$10.09	69.00 $\pm$13.88	65.49 $\pm$9.51
P_{Syst} [mmHg]	148.67 $\pm$30.68	134.31 $\pm$11.91	145.67 $\pm$20.64	140.09 $\pm$19.13	135.67 $\pm$21.16	140.74 $\pm$19.84
P_{Dist} [mmHg]	79.83 $\pm$5.88	80.54 $\pm$9.95	85.00 $\pm$13.39	79.09 $\pm$18.75	80.22 $\pm$13.42	81.01 $\pm$14.95
D_{m} [mm]	49.43 $\pm$3.88	50.35 $\pm$3.65	51.14 $\pm$4.68	49.65 $\pm$4.41	53.32 $\pm$4.01	50.53 $\pm$4.35
ΔD_{m} [%]	3.63 $\pm$1.34	3.22 $\pm$1.58	2.05 $\pm$1.07	2.13 $\pm$1.35	1.37 $\pm$1.08	2.31 $\pm$1.41
ΔV [%]	10.39 $\pm$5.22	8.88 $\pm$6.75	5.57 $\pm$3.94	5.55 $\pm$3.45	4.77 $\pm$3.34	6.35 $\pm$4.59
$\mathrm{Dist}_{\mathrm{Area}}$ [$10^{-3}\mathrm{mmHg^{-1}}$]	0.54 $\pm$0.49	1.16 $\pm$1.11	0.53 $\pm$0.34	0.44 $\pm$0.26	0.20 $\pm$0.43	0.56 $\pm$0.59
$\mathrm{Dist}_{\mathrm{Vol}}$ [$10^{-3}\mathrm{mmHg^{-1}}$]	1.55 $\pm$0.79	1.56 $\pm$1.49	1.09 $\pm$1.07	1.05 $\pm$0.74	0.72 $\pm$0.95	1.14 $\pm$1.01
L_{CL} [mm]	87.53 $\pm$11.50	84.00 $\pm$8.96	82.16 $\pm$10.38	88.83 $\pm$8.66	84.63 $\pm$8.78	85.80 $\pm$9.59
ΔL_{CL} [%]	3.67 $\pm$2.51	6.47 $\pm$3.44	5.14 $\pm$2.48	4.31 $\pm$2.81	2.45 $\pm$1.31	4.61 $\pm$2.86
L_{Circ} [mm]	17.61 $\pm$5.61	17.93 $\pm$2.79	17.60 $\pm$4.54	20.12 $\pm$3.92	19.26 $\pm$2.71	18.85 $\pm$4.04
D_{Circ} [mm]	76.41 $\pm$8.01	72.20 $\pm$7.18	70.37 $\pm$7.04	74.62 $\pm$5.46	71.30 $\pm$7.64	72.91 $\pm$6.75
$\theta_{\mathrm{AR,incr}}$ [°]	50.91 $\pm$13.49	56.83 $\pm$6.09	54.05 $\pm$10.80	58.28 $\pm$8.13	57.05 $\pm$7.22	56.29 $\pm$9.05
L_{Big} [mm]	113.03 $\pm$11.58	110.15 $\pm$9.09	107.82 $\pm$11.25	115.45 $\pm$10.79	112.66 $\pm$9.86	112.17 $\pm$10.84
L_{Small} [mm]	51.77 $\pm$7.74	44.87 $\pm$8.93	44.18 $\pm$6.34	46.65 $\pm$4.90	43.03 $\pm$6.11	45.71 $\pm$6.57
ΔL_{Big} [%]	4.34 $\pm$1.94	5.72 $\pm$3.63	4.25 $\pm$2.29	3.48 $\pm$2.25	2.13 $\pm$1.26	3.95 $\pm$2.57
$\Delta L_{\mathrm{Small}}$ [%]	6.36 $\pm$4.28	7.67 $\pm$4.44	6.14 $\pm$3.09	5.29 $\pm$4.17	4.09 $\pm$2.59	5.83 $\pm$3.87
$\theta_{\mathrm{CL,rot}}$ [°]	-12.5 $\pm$8.9	-5.07 $\pm$6.42	-6.55 $\pm$6.61	-3.50 $\pm$6.81	-2.07 $\pm$3.84	-5.03 $\pm$6.94
$D_{\mathrm{AR,m}}$ [mm]	42.08 $\pm$4.02	39.94 $\pm$6.97	41.13 $\pm$5.01	39.95 $\pm$5.03	41.81 $\pm$6.77	40.61 $\pm$5.44
$L_{\mathrm{AR,axial}}$ [mm]	-5.27 $\pm$2.06	-5.23 $\pm$2.87	-5.14 $\pm$2.21	-5.34 $\pm$2.93	-4.11 $\pm$2.36	-5.13 $\pm$2.60
$L_{\mathrm{AR,circ}}$ [mm]	7.54 $\pm$2.60	7.68 $\pm$2.01	7.40 $\pm$1.70	7.74 $\pm$2.12	5.27 $\pm$1.97	7.36 $\pm$2.11
$\theta_{\mathrm{AR,direc}}$ [$(-1)°$]	114.5 $\pm$7.5	113.3 $\pm$16.2	109.8 $\pm$16.1	113.1 $\pm$12.3	107.1 $\pm$17.5	111.7 $\pm$14.2

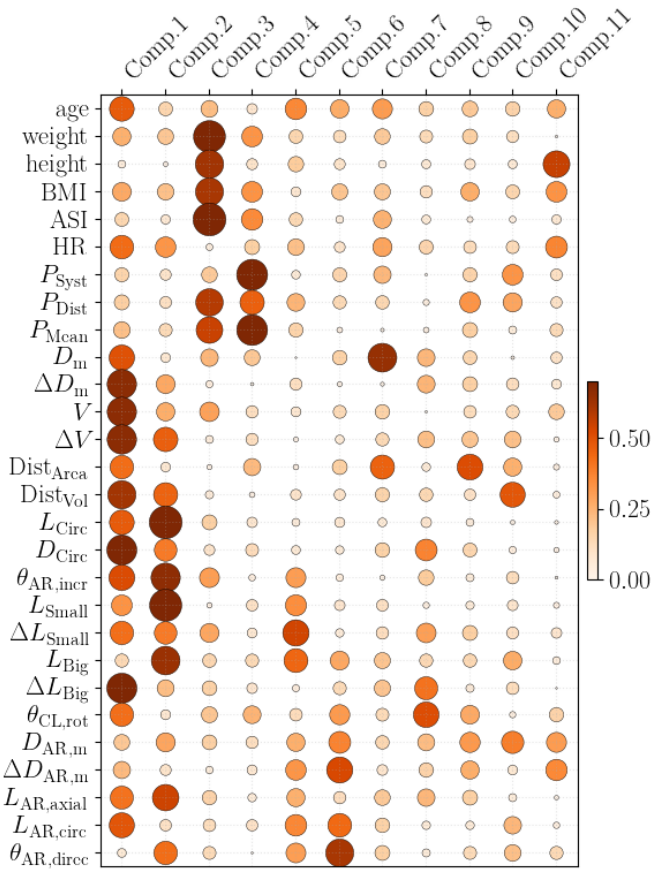

Fig. 12: Contribution of each variable to each principal dimension on the PCA.

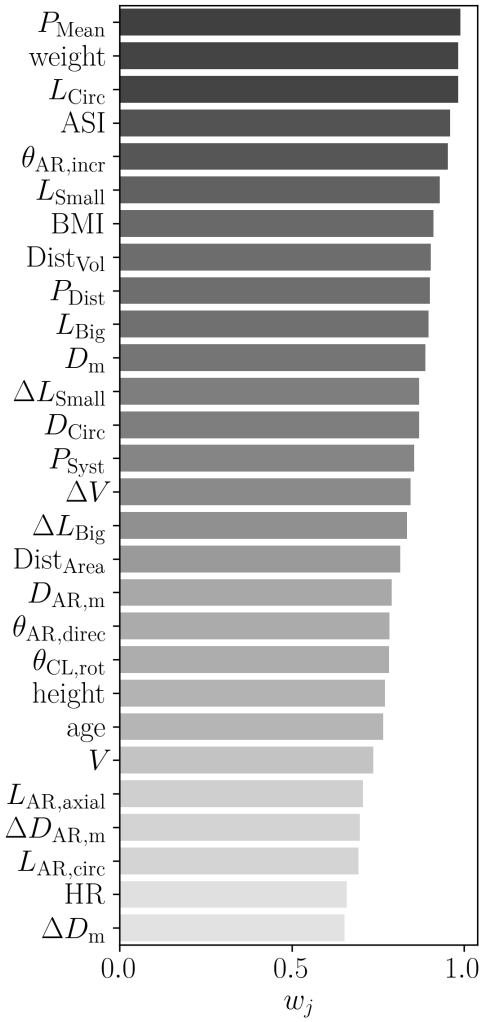

Fig. 13: w_j values for each variable, representing the total squared loadings of the variables within the principal components considered.

IV. Discussion

This study analysed ATAA motion using quantitative metrics to characterise its dynamic behaviour. Two main motion components were identified: radial motion, driven by arterial pressure variation, and non-rigid body motion, induced by heart motion. Our results show that non-rigid body motion dominates ATAA deformation, particularly in sections close to the AR, highlighting its potential significance for aneurysm biomechanics and haemodynamic impact.This is consistent with the prominence of the metrics that quantify AR motion ($L_{\mathrm{AR,axial}}$, $L_{\mathrm{AR,circ}}$).

In terms of radial motion, variations in diameter, volume, and distensibility were observed, with average values decreasing across age groups, suggesting age-related stiffening of the ATAA. Similar findings have been reported by Linden et al. [12], supporting the association between stiffness and ageing. Axial length variation (centreline length and AR axial displacement) followed a comparable pattern across patients, although the trend was less distinct and the small sample size in younger age groups limits the strength of this observation [27].

Figure 9 illustrates the temporal evolution of the centre-of-mass motion of the sinotubular plane and the diameter variation at the same location. Notably, the increase in diameter precedes the motion of the centre of mass, which suggests that pressure rises before the full displacement induced by cardiac contraction develops. Specifically, the time of peak centre-of-mass displacement had a mean temporal position of 43.30% of the cardiac cycle (SD 9.12%), whereas the time of peak maximum diameter at the sinotubular junction occurred earlier, with a mean of 37.66% (SD 15.94%). A temporal discrepancy between the beginning (0%) and end (100%) of the cardiac cycle can also be observed. This variation, present in the majority of patients, arises from the ECG-gated cCTA acquisition protocol since a mean heart rate is determined at the start of the examination, but slight variations in heart rate during the scan introduce misalignment between these time points. Although further refinement of the acquisition protocol could reduce this effect, the discrepancy does not significantly affect the present results, as the analysis primarily focuses on the systolic (35%) and diastolic (75%) phases rather than the exact cycle endpoints.

The AR was the segment most affected by heart motion. The AR centre of mass followed an elliptical trajectory with axial displacement, with direction stable across age groups

but magnitude decreasing with age. This agrees with previous reports on reduced aortic root mobility in older populations. A slight temporal offset was found between the maximum mean diameter (occurring earlier in the cycle) and the centre of mass motion peak (more temporally distributed), providing further insight into the interplay between root motion and radial expansion.

From a statistical perspective, PCA revealed that dynamic behaviours and ATAA volume primarily shaped the first component (19% variance), curvature features influenced the second (14.3%), and patient body size and arterial pressure dominated the third (12%) and fourth (7%), respectively. The most relevant metrics for explaining patient diversity were P_{Mean}, weight, L_{CL}, ASI, and L_{Circ}. Notably, maximum diameter (D_{m}) ranked only 11th in relevance, indicating that, in this cohort, it is a weaker discriminator of patient variability than other morphological and size-related metrics. While these parameters are not directly linked to rupture risk in the present study, their influence on patient variance suggests that they play a role in the underlying aneurysm biomechanics and may warrant further exploration for future risk stratification models. These findings support incorporating dynamic and geometric descriptors previously mentioned into future risk models rather than relying on geometry alone. They also highlight the importance of explicitly modelling aortic root motion in patient-specific Computational Fluid Dynamics (CFD) and Fluid-Structure Interaction (FSI) simulations, instead of prescribing purely circumferential expansion, to better capture the haemodynamic impact of ATAA dynamics. The patient distribution in PCA space showed that the first dimension better explained differences in BAV patients, while Tricuspid Aortic Valve (TAV) patients were more evenly distributed.

While the large dataset (82 patients x 21 time steps) provides statistical robustness against random segmentation errors, systematic biases in boundary detection could affect metrics involving high spatial gradients or small anatomical features. Concerning error propagation, the segmentation accuracy (Hausdorff distance of 0.656 mm) introduces measurement uncertainty into the deformation metrics. This error represents approximately 8 to 10% of the typical motion magnitudes observed, which is acceptable for identifying primary deformation patterns but may limit detection of smaller, localised deformations. The tracking algorithm presented a negligible error, with a Dice coefficient of 0.996 ± 0.0006 and a radius difference of 0.030 ± 0.0151 mm.

Limitations of this study include the under-representation of younger patients, which limits age-related comparisons. The deformation algorithm assumes negligible axial motion in the aortic arch and constant rotation increase simplifications that may underestimate dynamics. Additionally, the threshold-based semi-automatic segmentation method used is optimised for ATAA but less effective in other arterial regions. Finally, validation of observed motion patterns and PCA-derived parameters against clinical outcomes or rupture events was not possible in this dataset.

Our database is distributed unevenly across age groups, with a greater predominance of older patients. This is a common trend in the ATAA population due to disease progression

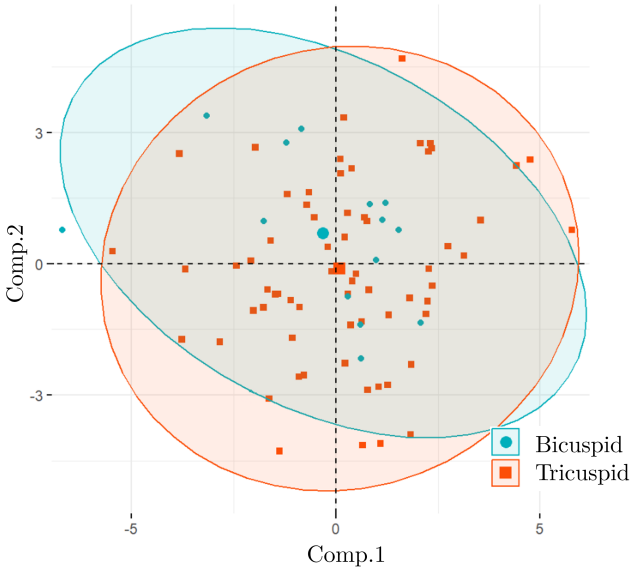

Fig. 14: AR morphology grouping on the first and second dimension.

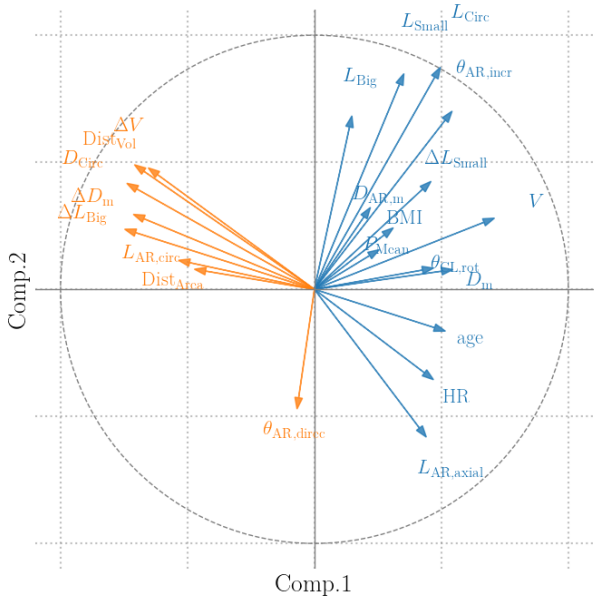

Fig. 15: Impact of each metrics on the first and second dimension. Some Variables with less impact were removed to improve readability.

in relation to ageing. It is important to note the significant presence of patients with BAV in younger age groups. This trend concurs with evidence that BAV is associated with earlier-onset aortic pathologies and higher aortic complication risk compared with TAV [28], and with reports of distinct haemodynamics and remodelling patterns in BAV [29, 30]. Nevertheless, our sample size is limited in the youngest groups to draw definitive conclusions.

V. Conclusions

In this study, we developed a segmentation framework based on a multi-view U-Net algorithm trained on semi-automatically segmented data. Additionally, we introduced a methodology to compute ATAA dynamics from cCTA scans.

The database provides a sample of the ATAA population, as no selection restrictions were applied, though younger groups are under-represented. Expanding the dataset would improve understanding of ATAA dynamics and disease progression. Methodological improvements are possible: the threshold-based semi-automatic segmentation performs well for ATAA but less so in other arterial regions, where training a U-Net on manually segmented datasets could yield better results. While the multi-view 2D U-Net works well for ATAA, its limited spatial context makes a 3D U-Net potentially more suitable for highly complex geometries. The deformation algorithm assumes negligible axial motion at the aortic arch and a smooth increase in rotation, simplifications that may underestimate dynamics and require further validation.

ATAA motion is influenced by arterial pressure and external factors. While internal pressure effects are well explained by numerical models, the role of aortic root motion on the ascending section remains under-explored. Future CFD and FSI simulations should incorporate this interaction to better capture haemodynamic impact.

A PCA of 82 patients and 28 variables (reduced via correlation analysis) retained 11 principal components (Kaiser criterion), explaining approximately 83.6% of the variance. The first component reflected dynamic behaviours, while the second was dominated by geometric markers. Combining component contributions, PCA highlighted pressure, body size, centreline length, ASI and centreline arc lengths as key descriptors, indicating patient size and aneurysm shape as central to ATAA characterisation in this cohort. Nonetheless, the selected metrics necessarily influence the PCA results; this was mitigated by the inclusion of a broad range of clinical and biomechanical variables but remains important to acknowledge.

Future work will include longitudinal analysis of the same patients over one year to capture disease progression, and integration of the measured deformation into mesh-morphing CFD models to assess haemodynamic effects compared to purely circumferential deformation in FSI simulations. Additionally, we plan to expand segmentation methods and explore patient-specific 3D motion modelling to refine both statistical and numerical analyses.

References

[1] Christian Olsson et al. “Thoracic Aortic Aneurysm and Dissection”. In: *Circulation* 114.24 (2006), pp. 2611–2618. DOI: 10.1161/CIRCULATIONAHA.106.630400.

[2] Katherine H Chau and John A Elefteriades. “Natural History of Thoracic Aortic Aneurysms: Size Matters, plus Moving beyond Size”. In: *Prog. Cardiovasc. Dis.* 56.1 (2013), pp. 74–80. DOI: 10.1016/j.pcad.2013.05.007.

[3] Jonathan Golledge et al. “Abdominal Aortic Aneurysm”. In: *Arterioscler. Thromb. Vasc. Biol.* 26.12 (2006), pp. 2605–2613. DOI: 10.1161/01.ATV.0000245819.32762.cb.

[4] Giampaolo Martufi et al. “Is There a Role for Biomechanical Engineering in Helping to Elucidate the Risk Profile of the Thoracic Aorta?” In: *Ann. Thorac. Surg.* 101.1 (2016), pp. 390–398. DOI: 10.1016/j.athoracsur.2015.07.028.

[5] Raimund Erbel et al. “2014 ESC Guidelines on the Diagnosis and Treatment of Aortic Diseases”. In: *Eur. Heart J.* 35.41 (2014), pp. 2873–2926. DOI: 10.1093/eurheartj/ehu281.

[6] Linda A. Pape et al. “Aortic Diameter > or = 5.5 Cm Is Not a Good Predictor of Type A Aortic Dissection: Observations from the International Registry of Acute Aortic Dissection (IRAD)”. In: *Circulation* 116.10 (2007), pp. 1120–1127. DOI: 10.1161/CIRCULATIONAHA.107.702720.

[7] Eric M. Isselbacher et al. “2022 ACC/AHA Guideline for the Diagnosis and Management of Aortic Disease: A Report of the American Heart Association/American College of Cardiology Joint Committee on Clinical Practice Guidelines”. In: *J. Am. Coll. Cardiol.* 80.24 (Dec. 13, 2022), e223–e393. DOI: 10.1016/j.jacc.2022.08.004.

[8] Martin Czerny et al. “EACTS/STS Guidelines for Diagnosing and Treating Acute and Chronic Syndromes of the Aortic Organ”. In: *Eur. J. Cardio-Thorac. Surg.* 65.2 (Feb. 2024), ezad426. DOI: 10.1093/ejcts/ezad426.

[9] Lucia Mazzolai et al. “2024 ESC Guidelines for the management of peripheral arterial and aortic diseases: Developed by the task force on the management of peripheral arterial and aortic diseases of the European Society of Cardiology (ESC) Endorsed by the European Association for Cardio-Thoracic Surgery (EACTS), the European Reference Network on Rare Multisystemic Vascular Diseases (VASCERN), and the European Society of Vascular Medicine (ESVM)”. In: *European Heart Journal* 45.36 (Aug. 2024), pp. 3538–3700. DOI: 10.1093/eurheartj/ehae179.

[10] Salvatore Pasta et al. “In Vivo Strain Analysis of Dilated Ascending Thoracic Aorta by ECG-Gated CT Angiographic Imaging”. In: *Ann. Biomed. Eng.* 45.12 (Dec. 2017), pp. 2911–2920. DOI: 10.1007/s10439-017-1915-4.

[11] Federica Cosentino et al. “Statistical Shape Analysis of Ascending Thoracic Aortic Aneurysm: Correlation between Shape and Biomechanical Descriptors”. In: *J. Pers. Med.* 10.2 (Apr. 22, 2020), p. 28. DOI: 10.3390/jpm10020028.

[12] Klaas Vander Linden et al. “Stiffness Matters: Improved Failure Risk Assessment of Ascending Thoracic Aortic Aneurysms”. In: *JTCVS Open* 16 (Dec. 1, 2023), pp. 66–83. DOI: 10.1016/j.xjon.2023.09.008.

[13] Nicasius S Tjahjadi et al. “Three-Dimensional Assessment of Ascending Aortic Stiffness, Motion, and

Growth in Ascending Thoracic Aortic Aneurysm". In: *European Heart Journal - Imaging Methods and Practice* 3.1 (Jan. 2025), qyae133. DOI: 10.1093/ehjimp/qyae133.

[14] Ga-Young K. Suh et al. "Ascending Aortic Endograft and Thoracic Aortic Deformation After Ascending Thoracic Endovascular Aortic Repair". In: *Journal of Endovascular Therapy* 32.1 (Feb. 2025), pp. 7–17. DOI: 10.1177/15266028231168351.

[15] Olaf Ronneberger, Philipp Fischer, and Thomas Brox. "U-Net: Convolutional Networks for Biomedical Image Segmentation". In: *Medical Image Computing and Computer-Assisted Intervention – MICCAI 2015*. Ed. by Nassir Navab et al. Cham: Springer International Publishing, 2015, pp. 234–241. DOI: 10.1007/978-3-319-24574-4_28.

[16] Rehan Raza et al. "dResU-Net: 3D Deep Residual U-Net Based Brain Tumor Segmentation from Multimodal MRI". In: *Biomed. Signal Process. Control* 79 (Jan. 1, 2023), p. 103861. DOI: 10.1016/j.bspc.2022.103861.

[17] Muhammad Imran et al. *CIS-UNet: Multi-Class Segmentation of the Aorta in Computed Tomography Angiography via Context-Aware Shifted Window Self-Attention*. Jan. 23, 2024. DOI: 10.48550/arXiv.2401.13049. Pre-published.

[18] Jiasong Chen et al. *A 3D Image Segmentation Study of U-Net on CT Images of the Human Aorta with Morphologically Diverse Anatomy*. Oct. 3, 2024. DOI: 10.1101/2024.10.02.616348. Pre-published.

[19] Haben Berhane et al. "Fully Automated 3D Aortic Segmentation of 4D Flow MRI for Hemodynamic Analysis Using Deep Learning". In: *Magn. Reson. Med.* 84.4 (2020), pp. 2204–2218. DOI: 10.1002/mrm.28257.

[20] Simone Bonechi et al. "Segmentation of Aorta 3D CT Images Based on 2D Convolutional Neural Networks". In: *Electronics* 10.20 (20 Jan. 2021), p. 2559. DOI: 10.3390/electronics10202559.

[21] Alice Fantazzini et al. "3D Automatic Segmentation of Aortic Computed Tomography Angiography Combining Multi-View 2D Convolutional Neural Networks". In: *Cardiovasc Eng. Tech.* 11.5 (Oct. 1, 2020), pp. 576–586. DOI: 10.1007/s13239-020-00481-z.

[22] Stéfan van der Walt et al. "Scikit-Image: Image Processing in Python". In: *PeerJ* 2 (June 19, 2014), e453. DOI: 10.7717/peerj.453.

[23] C. Bane Sullivan and Alexander A. Kaszynski. "PyVista: 3D Plotting and Mesh Analysis through a Streamlined Interface for the Visualization Toolkit (VTK)". In: *J. Open Source Softw.* 4.37 (May 19, 2019), p. 1450. DOI: 10.21105/joss.01450.

[24] Luca Antiga et al. "An image-based modeling framework for patient-specific computational hemodynamics". In: *Med Biol Eng Comput* 46.11 (Nov. 2008), pp. 1097–1112.

[25] Ga-Young Suh et al. "Aortic Arch Vessel Geometries and Deformations in Patients with Thoracic Aortic Aneurysms and Dissections". In: *J. Vasc. Interv. Radiol.* 25.12 (Dec. 2014), pp. 1903–1911. DOI: 10.1016/j.jvir.2014.06.012.

[26] I.T. Jolliffe. *Principal Component Analysis*. 2nd. Springer Series in Statistics. New York: Springer-Verlag, 2002. DOI: 10.1007/b98835.

[27] Caitlin Martin et al. "Age-Dependent Ascending Aorta Mechanics Assessed Through Multiphase CT". In: *Annals of Biomedical Engineering* 41.12 (Dec. 2013), pp. 2565–2574. DOI: 10.1007/s10439-013-0856-9.

[28] Michael A. Borger et al. "2018 AATS Consensus Guidelines: Bicuspid Aortic Valve–Related Aortopathy". In: *J. Thorac. Cardiovasc. Surg.* 156.2 (2018), e41–e74. DOI: 10.1016/j.jtcvs.2018.02.115.

[29] Salvatore Pasta et al. "Difference in Hemodynamic and Wall Stress of Ascending Thoracic Aortic Aneurysms with Bicuspid and Tricuspid Aortic Valve". In: *J. Biomech.* 46.10 (2013), pp. 1729–1738. DOI: 10.1016/j.jbiomech.2013.03.029.

[30] Valentina Agnese et al. "Patterns of Ascending Aortic Dilatation and Predictors of Surgical Replacement of the Aorta: A Comparison of Bicuspid and Tricuspid Aortic Valve Patients over Eight Years of Follow-Up". In: *J. Mol. Cell. Cardiol.* 135 (February 2019), pp. 31–39. DOI: 10.1016/j.yjmcc.2019.07.010.